Materials Science Forum
ISSN: 1662-9752, Vol. 1182, pp 59-71
doi:10.4028/p-zhZXT4
© 2026 The Author(s). Published by Trans Tech Publications Ltd, Switzerland.
Submitted: 2026-01-19
Revised: 2026-02-18
Accepted: 2026-02-18
Online: 2026-04-10

Machine Learning-Based Prediction of Forming-Induced Defects in Flax Woven Fabrics Using 3D Scanning and Haralick Texture Features

Margoto Olivia H.[1,a*], Batouei Mohammad A.[1,b], Yang Victor[1,c], Abdin Yasmine[2,d*] and Milani Abbas S.[1,e]

[1]School of Engineering, University of British Columbia, Kelowna, Canada

[2]Department of Materials Engineering, University of British Columbia, Vancouver, Canada

[a*]olivia.margoto@gmail.com, [b]amin.batouei@gmail.com, [c]vy@student.ubc.ca, [d]yasmine.abdin@ubc.ca, [e]abbas.milani@ubc.ca

Keywords: flax woven fabrics, forming-induced defect prediction, 3D scanning, haralick features extraction and prediction, Monte Carlo cross-validation.

Abstract. Natural fiber-reinforced composites offer lightweight and sustainable alternatives for automotive and aerospace applications. However, similar to synthetic composite options, forming-induced defects such as wrinkles can reduce targeted performance. Predicting these defects is particularly challenging for natural fiber reinforcements due to the inherent variability in the fiber geometry and ensuing fabric properties. This study applies a machine learning approach to predict formability in flax woven fabrics (2×2 twill and biaxial non-crimp) using a glass fabric as a synthetic fabric reference. The fabrics' shear, bending, tensile, and friction behaviors were experimentally characterized to capture forming-relevant mechanical properties. The fabrics were subsequently formed in single-, dual-, and triple-layer configurations over a square tool, followed by 3D scanning to quantify wrinkle distributions. Forming-induced surface deformations were transformed into grayscale maps, from which Haralick texture features were extracted. Combined with the fabric design parameters such as weave, orientation, number of layers, grammage, and thickness, the mechanical properties features were used to train linear regression models, reliably predicting select Haralick features, cross-validated using Monte Carlo simulations. Results showed that flax twill reinforcements exhibited the lowest formability, while the glass fabric formed smoothly, and biaxial non-woven fabric showed primarily localized folds. Increasing the fabric orientation from 0° to 45° improved forming performance for most woven reinforcements; but not the biaxial non-woven alternative. Linear regression models accurately predicted the defect severity via homogeneity (R^2 = 0.81) and dissimilarity (R^2 = 0.73) texture features, demonstrating that integrating texture-based image analysis with fabric parameters and mechanical properties provides a promising machine-learning-based framework for predicting forming performance of fabric-reinforced composites.

Introduction

Woven and non-woven fabric–reinforced composites are widely used in automotive and aerospace applications, among others, due to their low weight, high strength, and good formability [1,2]. In Liquid Composites Molding (LCM), this formability is critical, as dry reinforcements must conform to complex tool geometries prior to resin injection [3,4]. Inadequate control of the forming stage can lead to defects such as out-of-plane wrinkling, in-plane waviness, tow buckling, fiber fracture, and slippage, which may ultimately result in part rejection [2,5]. Consequently, detailed characterization of fabric behavior under different deformation modes is essential to understand the mechanisms behind forming-induced defects. During forming, the fabric reinforcements often undergo in-plane shear, biaxial extension, inter-ply and tool–ply friction, bending, and compaction, with intra-, inter-ply shear and ply bending playing dominant roles in enabling the lay-up conformance to single- and double-curvature geometries [2,4,6–9].

Fiber architecture and physical properties further influence the defect formation [10]. For example, biaxial Non-Crimp Fabrics (NCFs) provide high tensile and flexural stiffness but are sensitive to stitching characteristics (e.g., density, pattern, thread, and orientation) [11–14], whereas woven

This article is an open access article under the terms and conditions of the Creative Commons Attribution (CC BY) license (https://creativecommons.org/licenses/by/4.0)

fabrics introduce crimp that modifies in-plane shear behavior [10]. In natural fiber reinforcements, additional complexity arises from inherent material variability and yarn heterogenous structure. Flax flat yarns, e.g., composed of segmented elementary fibers bonded with adhesives, exhibit high lateral stiffness, making them prone to tow buckling during forming, while removing adhesives after weaving further increases strain and reduces tow strength [15,16]. Physical parameters such as areal density and fiber distribution also affect deformability, with higher-density flax non-woven mats showing improved preforming behavior [17].

Geometrical and processing factors also play a key role in forming outcomes. For instance, forming over square-box tools has been shown to induce severe shear and wrinkling due to sharp corners and quasi-inextensible fiber paths, whereas cylindrical mold geometries distribute deformation more uniformly [4,18,19]. Process defects substantially degrade the mechanical performance of the final part, with wrinkles reaching 20–60% of the nominal laminate thickness reported to reduce cured part strength by 50–70% [20]. Modifications to tool and blank-holder designs can help reduce defects (e.g., adding risers to increase fabric tension), though optimal configurations remain highly case-dependent due to the complex fabric–tool interactions [21].

Understanding and predicting forming behavior is therefore critical for improving fabric composites manufacturability and quality. Machine Learning (ML) approaches guided by experimental and simulation data have only recently shown promise for predicting drapability behavior of different composite materials (including fabrics), enabling faster defect detection, parameter optimization, and quality prediction through data-driven methods [22,23]. For instance, ML approaches have been successfully used to infer optimal forming parameters from laminate images [24], optimize forming parameters through reinforcement learning [22], classify defective parts with high accuracy [25], and support automated inspection and real-time control in advanced manufacturing processes [26–28]. Despite these advancements, most of current ML applications have focused on synthetic fiber–reinforced composites [22–26,28], leaving a gap in applying data-driven approaches to forming-induced defects in natural fiber woven reinforcements.

This study addresses this gap by developing a supervised machine learning framework to predict the formability of a set of commercial flax fiber woven reinforcements, with glass fiber fabric also used as a reference. Fabric geometrical parameters and their mechanical properties serve as model inputs, while forming-induced defects are quantified using Haralick texture metrics, extracted digitally from post-forming wrinkle maps. As a proof of concept, formability is predicted using linear regression due to the limited dataset, and model robustness is evaluated through Monte Carlo cross-validation.

Methodological Details

Materials.

Three commercial flax reinforcements were selected: a 250 g/m² 2×2 twill fabric from Lingrove (FTW250), a 367 g/m² 2×2 twill fabric from Rock West Composites (FTW367), and a 350 g/m² ampliTex® biaxial non-crimp fabric from Bcomp (FBX350). A 280 g/m² 2×2 twill glass fiber fabric from Easy Composites was included as a synthetic reference material for comparison. The twill flax fabric is made from flat tows, the biaxial NCF from spun yarns, and the glass fabric from rovings. The main physical properties of these test materials are listed in Table 1.

Table 1. Specifications of the tested flax fabrics.

Fabric code	FTW250	FTW367	FBX350	GTW280
Material (type)	Flax	Flax	Flax	Glass
Weave (type)	2x2 Twill	2x2 Twill	Biaxial NCF	2x2 Twill
Areal weight (g/m^2)	250	367	350	280
Thickness (mm)	0.78 ± 0.03	1.29 ± 0.05	0.97 ± 0.03	0.29 ± 0.01
Tow orientation (°)	0/90	0/90	± 45	0/90
Stitch Orientation (°)	-	-	90	-
Number of warp yarns per cm	4	3.5	14	7
Number of weft yarns per cm	4	3.5	8	8

An overview of the designed workflow for predicting fabric formability is presented in Fig. 1, illustrating the sequence from the material selection and mechanical characterization, through 3D forming and post-forming surface mapping via a handled scanner, to wrinkle quantification, Haralick feature extraction for regression modeling.

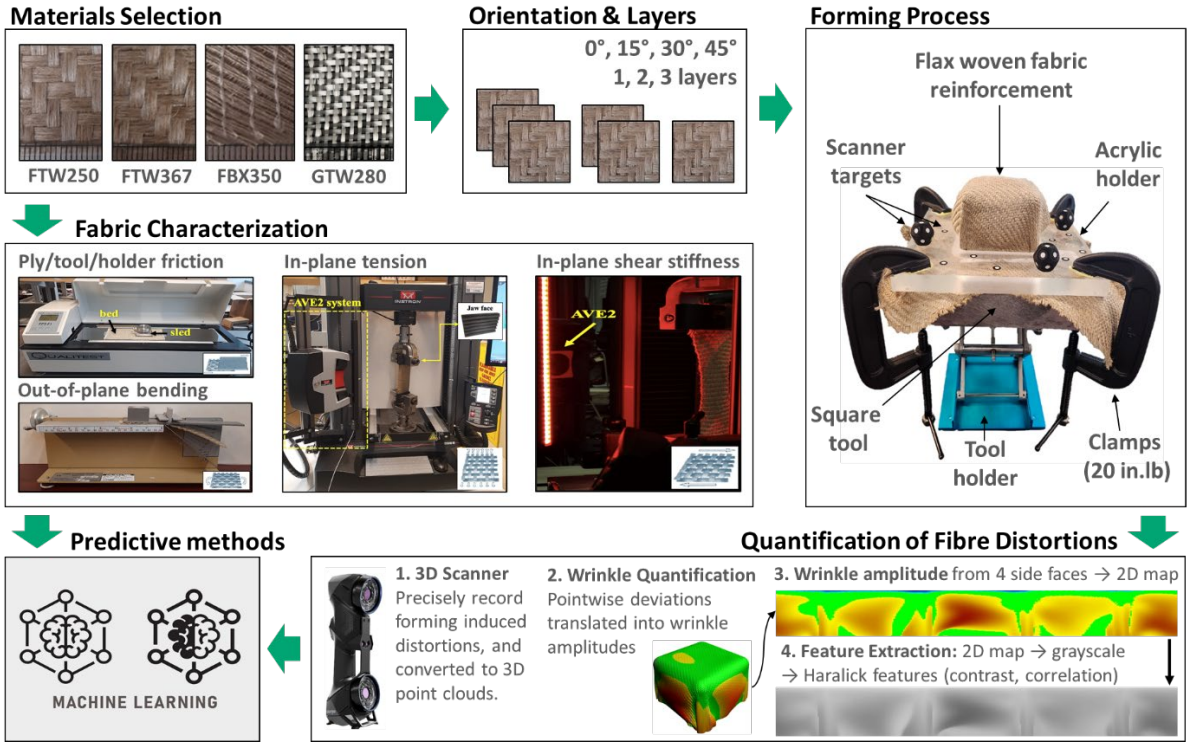

Fig. 1. Overall workflow for the formability prediction, summarizing materials, mechanical characterization, 3D forming, data acquisition, and Haralick feature extraction for machine learning modeling.

Mechanical characterization of the reinforcements.

Mechanical characterization of the selected reinforcements included friction, bending, tensile, and shear behavior, reflecting the deformations these fabrics undergo during complex 3D forming [3].

Friction Characterization.

Ply-ply, ply-tool, and ply-holder friction coefficients were measured using a Friction Tester (Labthink International Inc., USA). For ply-ply tests, fabric specimens (250 × 130 mm on the bed, 63.5 × 63.5 mm on the sled) were used. Ply-tool and ply-holder tests employed aluminum and acrylic plates on the bed, respectively. Tests were conducted at 4 mm/min under ~5 N force and repeated five times per configuration for consistency.

Effective out-of-plane bending.

The bending stiffness of flax and glass fabrics was measured using a Peirce cantilever tester (Taber Industries, USA) on nine specimens per fabric (200 × 25 mm) [29]. Each fabric's ability to bend under its own weight was evaluated by sliding strips over a platform edge until they bent at approximately 41.5°. Overhang length and fiber width were recorded, and bending length and flexural rigidity, D (N.mm), were calculated following ASTM D1388 [30]. Then, the effective out-of-plane bending (D_{eff}) at specific fabric angles θ (as illustrated in Fig. 2) was calculated as per Eq. 1 [31]:

$$D_{eff} = D\,cos^2\,\theta \tag{1}$$

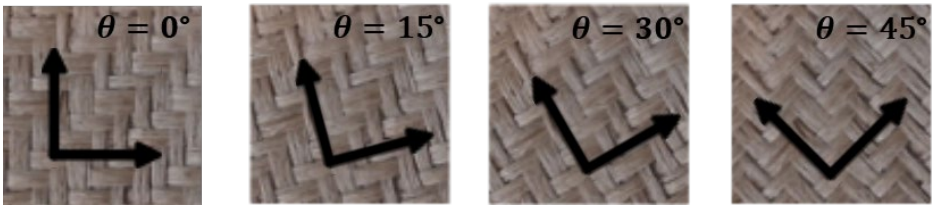

Fig. 2. Schematic of fabric orientation used to calculate effective mechanical properties. The orientation angle θ is measured relative to the tool square corner, and relative to the loading direction for tension.

Effective in-plane tension. Five specimens (250 mm × 75 mm) for each fabric configuration were tested in uniaxial tension using an Instron 5969 at 5 mm/min with a 150 mm gauge length, and wave-profile jaws were used to prevent slippage [32–34]. The 2×2 twill fabrics were tested at 0/90°, and the biaxial non-crimp fabric with its stitch direction aligned to the loading axis. The effective modulus for each fabric orientation was calculated from the initial linear region of the stress–strain curve [35–37] as per Eq. 2:

$$E_{eff} = (cos^4\,\theta + sin^4\,\theta)\,E \tag{2}$$

where θ is the fiber (or stitch) orientation relative to the loading direction, E_{eff} is the unidirectional fiber modulus and E is the effective in-plane modulus in the loading direction, assuming a balanced fabric architecture.

In-plane shear stiffness.

The in-plane shear behavior of the textile reinforcements was evaluated using bias extension tests. Rectangular specimens (210 × 55 mm) with yarns at 45º to the fiber (local) tension direction were clamped in flat rubber-coated jaws with a 110 mm gauge length and tested three times per fabric on an Instron 5969 at 5 mm/min [4,32]. Normalized shear forces F_{sh} (N/mm) and shear angles γ (º) were calculated as described in [38]. The shear modulus was taken at a 40º shear angle, consistent with [4].

3D forming setup.

An experimental 3D forming setup was developed in-house for rapid yet repeatable data collection on the forming behavior of the woven fabrics, as shown in Fig. 1. The setup consisted of a square-box tool (112 mm width) and a transparent acrylic fabric holder (25 mm thick). Surface geometry and forming-induced defects were captured using a Handyscan Black Elite 3D scanner (Creaform Inc., Canada) with an accuracy of 0.025 mm. Fabric specimens (45 cm × 45 cm) were cut according to predefined fiber orientations (0°, 15°, 30°, and 45°) and layer configurations (1, 2, and 3 layers).

During forming, the fabric holder was manually displaced at an approximately constant speed to drape the fabric over the tool and subsequently clamped under a controlled torque of 20 in·lb.

Haralick feature extraction for predictive models.

3D scanned surface after each forming experiment was imported as point clouds using the Open3D Python library. Individual layers were extracted by selecting points within a defined tolerance of the target planes (e.g., all x-coordinates within 0.1 mm of the target), reducing the 3D data to 2D representations for surface analysis. To isolate forming-induced deformations, the scanned formed-fabric surface was decoupled from the underlying square-box tool geometry. The ideal tool surface, representing the nominal geometry in the absence of wrinkles, was modeled using the Superellipse Lamé curve (Eq. 3) [39]:

$$\left|\frac{x-\mathrm{a}}{r_a}\right|^{\mathrm{n}} + \left|\frac{y-\mathrm{b}}{r_b}\right|^{\mathrm{n}} = 1 \tag{3}$$

where the x and y are the Cartesian coordinates of points on the tool surface. The tool is centered at the origin ($a = b = 0$), has a width of 112 mm ($r_a = r_b = \frac{1}{2} width$), and a corner roundness defined by $n = 12\ mm$.

The Cartesian coordinates of both the scanned surface and the ideal tool geometry were converted into polar coordinates with respect to the tool center. In this representation, α parameterizes the position along the tool perimeter and r represents the radial distance from the tool center, as shown in Fig. 3. Forming-induced deformations were obtained by subtracting the ideal radius from the measured radius at each α, producing a one-dimensional deformation profile that captures local forming-induced surface deviations. The use of α provides a natural ordering of points along the surface, enabling the generation of structured 1D profiles suitable for Haralick feature analysis.

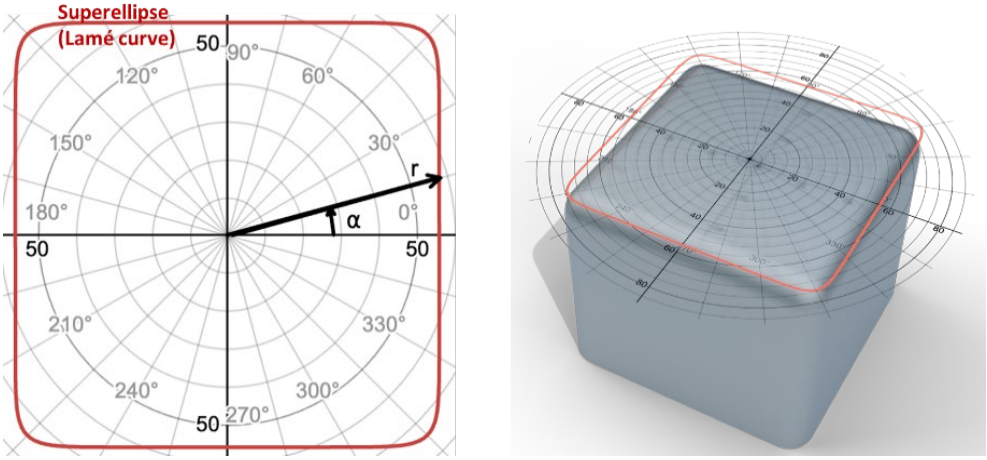

Fig. 3. Polar representation (r, α) of the square tool, converting the 2D scanned surface into a structured 1D profile suitable for Haralick texture analysis.

To visualize these deformations across the lateral surfaces, 2D maps were generated by compiling unfolded vertical face profiles into grayscale images, where intensity represents deviation magnitude. The top surface was excluded for simplicity. These deformation maps, at each surface of the formed box, were processed into Gray Level Co-Occurrence Matrices (GLCMs) and normalized to extract Haralick features, including ASM, Contrast, Correlation, Dissimilarity, Energy, and Homogeneity [40,41]. Combined with fabric geometrical parameters (weave, orientation, number of layers, grammage, thickness) and mechanical properties (Table 2), these features were used to train linear regression models to predict fabric formability, with Haralick features representing wrinkle patterns.

The linear regression dataset comprised 48 samples. Given this relatively small dataset and the need for interpretable relationships between fabric parameters and texture-based defect metrics, linear regression method was selected as a baseline/preliminary supervised learning approach due to its simplicity and prior literature use in composite defect detection prediction [23]. An independent test

set corresponding to 30% of the data was held out for final model evaluation. The remaining 70% of the samples were used for model training and assessed using Monte Carlo cross-validation with 10 random resampling iterations to evaluate model robustness [42]. Model performance was quantified using the coefficient of determination (R^2) and the Mean Absolute Error (MAE).

Results and Discussion

Mechanical characterization of the reinforcements.

The mechanical properties of the flax and glass fiber reinforcements are summarized in Table 2 for the 0/90° orientation, and the arrows indicate literature-supported trends associated with reduced forming-induced wrinkles. For the two 2×2 twill woven flax fabrics, the increase in areal weight from FTW250 to FTW367 resulted in a higher Young's modulus, consistent with the presence of more load-bearing fibers per unit area in FTW367. The glass fiber reinforcement (GTW280) remained substantially stiffer (3.29 GPa) than all flax reinforcements. As reported in the earlier literature [4], lower tensile stiffness promotes greater in-plane elongation, which can facilitate draping over complex geometries by lowering the induced shear angle.

It is important to emphasize that the continuous fiber textile reinforcements investigated in this study are composed of relatively stiff yarns compared to knitted reinforcements or stretch-broken fibers [4]. Achieving a double-curved geometry therefore necessitates substantial in-plane shear deformation, as shear is one of the dominant mechanisms enabling the transition from two-dimensional plies to three-dimensional formed components [6,18,43]. Consistent with this, FTW367 (higher areal weight) exhibited higher shear stiffness than FTW250. This trend aligns with observations in jute fabrics, where low-density architectures allow greater yarn mobility and rotation, enabling larger deformations under lower axial forces [44]. Interestingly, the shear stiffness of the glass reinforcement GTW280 was similar to that of FTW250, despite the significant difference in tensile modulus.

Table 2. Mechanical properties of the tested fabric reinforcements at 0/90° orientation.

Fabric (type)	↓ Young's Modulus (GPa)	↓ Shear Stiffness at 40° ($N.mm^{-1}$)	↑ Bending Stiffness (N.mm)	↓ Friction Ply/ Mold Dynamic coefficient
FTW250	0.24 ± 0.08	0.008 ± 0.001	1.47 ± 0.16	0.17 ± 0.00
FTW367	0.46 ± 0.11	0.021 ± 0.002	1.61 ± 0.47	0.16 ± 0.00
FBX350	0.57 ± 0.15	0.069 ± 0.035	1.04 ± 0.09	0.15 ± 0.00
GTW280	3.29 ± 0.34	0.012 ± 0.002	0.07 ± 0.01	0.22 ± 0.01

* Arrows indicate literature-supported trends associated with reduced forming-induced wrinkles [2–4].

Regarding bending behavior, the flax twill fabrics displayed comparable flexural rigidity, while the biaxial NCF (FBX350) exhibited lower bending stiffness. The glass fabric showed the lowest bending stiffness despite its high tensile modulus, which was also observed by Bai et al. [4]. Literature indicates that higher bending stiffness generally contributes to improved drapability and reduced wrinkling in dry textiles, as the ply with the lowest bending stiffness tends to wrinkle first during forming [4,45,46].

For ply–tool friction, all flax reinforcements showed similarly low dynamic and static coefficients, whereas the glass fabric exhibited a noticeably higher coefficient. When considering forming-induced wrinkling in dry reinforcements, low friction between the ply tool can facilitate smoother deformation as the dry reinforcement shapes around complex tooling geometries, reducing the likelihood of wrinkles.

3D forming Experiments.

The experimental evaluation of single- and triple-layer reinforcements formed into the square shape involved analyzing 3D surface deformations across multiple orientations. The results, summarized in Fig. 4, highlight clear material- and orientation-dependent differences in formability. In the single-layer condition, the woven reinforcements FTW250, FTW367, and GTW280 exhibited their most

severe forming-induced defects at the 0° orientation, where large out-of-plane wrinkles and distortions were consistently observed.

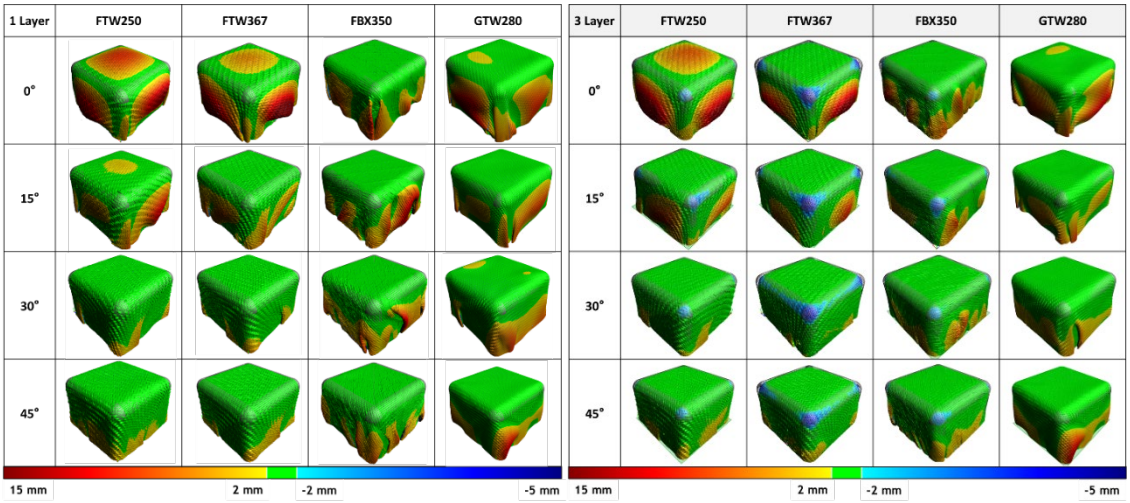

Fig. 4. 3D surface deformation of the reinforcements formed into a square shape and scanned: single-layer configuration (left) and three-layer configuration (right). Colors indicate the deformation magnitude in millimeters, as shown by the scale below each image.

For the biaxial NCF (FBX350), the poorest performance occurred at 15°. Among all materials, the flax twill reinforcements showed the lowest formability, displaying bulky, highly pronounced wrinkles with amplitudes reaching up to 15 mm across the five evaluated faces. In contrast, the glass fiber reinforcement formed more efficiently (with minimal defects) under the same conditions. Although the biaxial NCF exhibited surface deformation of similar magnitude to the flax twills, the resulting defects were primarily localized folds rather than large-scale out-of-plane distortions.

Increasing the fabric orientation from 0° to 45° markedly improved the forming response of most woven reinforcements in the single-layer setup. FTW367 showed the greatest improvement at 30° and 45°, where the formed shapes were noticeably smoother and exhibited fewer wrinkles. By comparison, the FBX350 NCF showed little variation in deformation across the tested orientations. This relative orientation independence is likely due to its higher in-plane stiffness, lower bending compliance, and reduced inter-ply friction, which together restrict its ability to conform to double-curved shapes [4].

When comparing single-layer to three-layer configurations, the forming behavior of GTW280 remained largely unchanged across all orientations, indicating a low sensitivity to layer count. For FTW250 at 0°, the deformation patterns also remained similar between one- and three-layer forming. In most other cases, however, FTW250, FTW367, and FBX350 formed more effectively in the three-layer configuration. The thicker laminate generated greater clamping tension during forming, which helped stabilize the fabric and reduce defect severity. Among all reinforcements, FTW367 again demonstrated the best performance at 30° and 45°, producing the smoothest surfaces with the smallest wrinkles. Localized fiber compression was observed at the corners of the formed shape, visible as concentrated regions of deformation. Notably, while folds and other surface defects were much more pronounced in single-layer flax NCF compared to the glass fabric, the difference between the two materials diminished substantially in the three-layer configuration.

Haralick feature extraction for predictive models.

The Haralick features extracted from the deformation maps (Fig. 4) were used to assess the predictive capability of linear regression models for fabric formability. Table 3 summarizes the model performance in terms of R^2 and MAE, reported as average ± standard deviation across the 10 Monte Carlo cross-validation runs. For completeness, texture features such as Contrast and ASM were evaluated in the methodology but did not contribute meaningfully to model predictability and are therefore not included in the remaining sections of this study.

Table 3. Average linear regression models' performance obtained across Monte Carlo cross-validation runs for the prediction of different Haralick texture features (dependent variables).

Haralick Features		Correlation	Dissimilarity	Energy	Homogeneity
R-square (R^2)	Training	0.74 ± 0.03	0.86 ± 0.03	0.76 ± 0.03	0.90 ± 0.03
	Testing	0.57 ± 0.16	0.73 ± 0.12	0.67 ± 0.11	0.81 ± 0.10
	All dataset	0.71 ± 0.01	0.84 ± 0.01	0.75 ± 0.01	0.88 ± 0.01
Mean Absolute Error (MAE)	Training	0.00 ± 0.00	0.03 ± 0.00	0.01 ± 0.00	0.01 ± 0.00
	Testing	0.00 ± 0.00	0.04 ± 0.00	0.01 ± 0.00	0.01 ± 0.00
	All dataset	0.00 ± 0.00	0.03 ± 0.00	0.01 ± 0.00	0.01 ± 0.00

Among the evaluated texture features, dissimilarity and homogeneity were predicted most accurately by linear regression, with Monte Carlo–averaged testing R^2 up to 0.81, compared to 0.57–0.67 for correlation and energy. Fig. 5 shows a prediction plot from a single Monte Carlo iteration along with the R^2 values from all 10 cross-validation runs, illustrating both model performance and stability under repeated resampling.

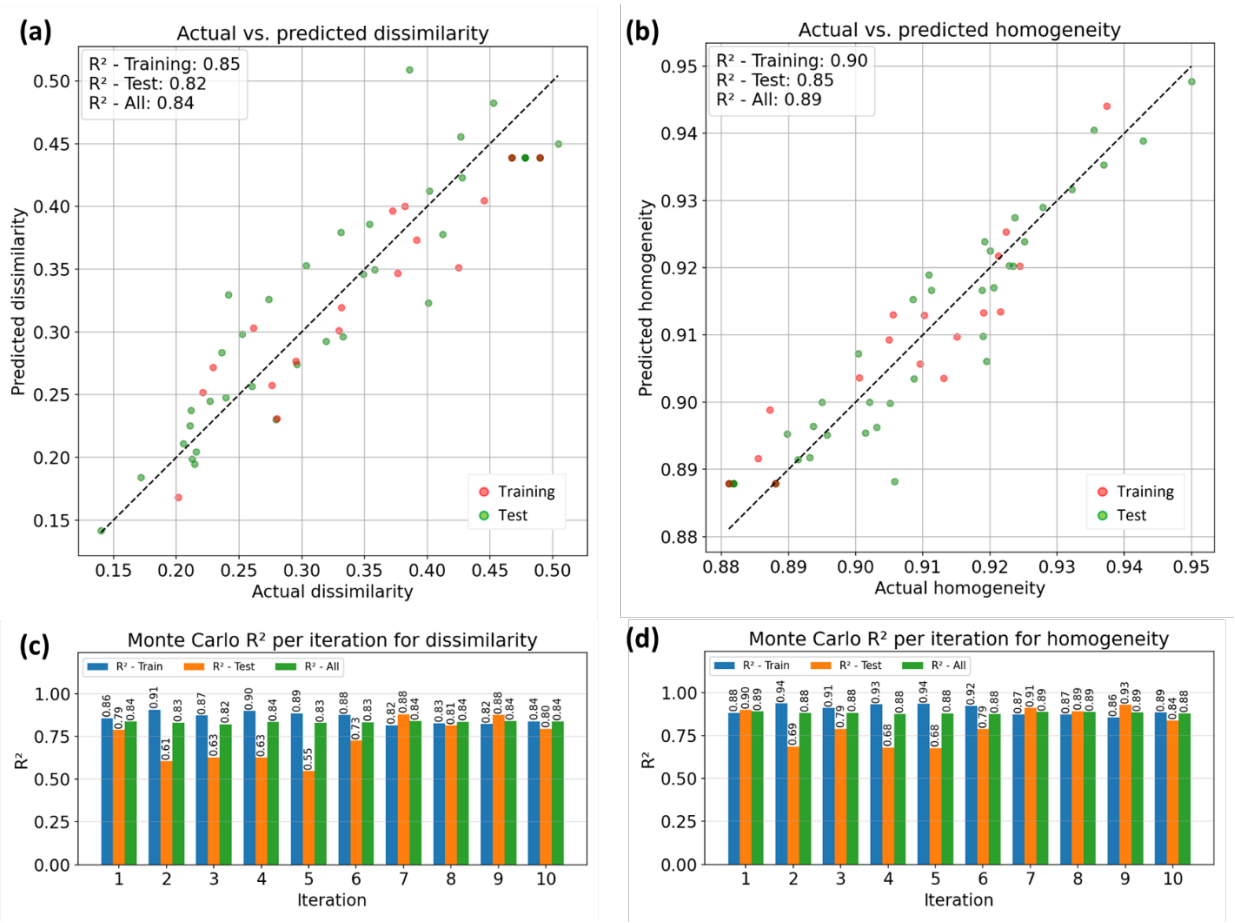

Fig. 5. Linear regression for Haralick features: (a) actual vs. predicted dissimilarity, (b) actual vs. predicted homogeneity, (c) Monte Carlo R^2 per iteration for dissimilarity, (d) Monte Carlo R^2 per iteration for homogeneity.

Theoretically, the homogeneity measures how similar neighboring pixel intensities are, based on the gray-level co-occurrence matrix [40,41]. Values close to the GLCM diagonal indicate a uniform texture, while lower values indicate more variation. Consequently, accurate prediction of homogeneity provides valuable insight into the consistency of wrinkle formation on the formed surface. In this study, a trend was observed in which lower homogeneity values corresponded to pronounced wrinkles (mainly formed along the square-tool sides), suggesting that this Haralick

feature can provide a quantitative indicator of surface quality and forming consistency in flax-reinforced composites.

Dissimilarity measures the average intensity difference between a pixel and its neighbors across the image, thereby capturing variations in gray-level pairs. Higher dissimilarity values indicate greater texture variation, and hence more severe surface defects [47–49]. Accurate prediction of this metric enables direct comparison of wrinkle intensity between different forming materials. Notably, dissimilarity was found to capture both defect severity and fabric architecture effects: draping of glass fiber reinforcement was associated with lower dissimilarity values, whereas higher values corresponded to the FBX350 reinforcement. This dissimilarity feature provided the second-best prediction accuracy, with an average R^2 of 0.73 on the test sets over 10 Monte Carlo cross-validation runs.

The FBX350 forming was observed to be clustered by low Haralick correlation values. Although the R^2 for correlation was relatively low ($R^2 < 0.57$ for testing dataset), it still shows potential to capture differences in wrinkle-pattern progression across the forming surface, where long, narrow folds dominate. This reflects how intrinsic material properties influence wrinkle formation.

The energy among Haralick features also exhibited a clear relationship with fabric orientation and forming-induced defects. Lower energy values at smaller orientation angles (0° and 15°) were associated with increased defect severity, whereas higher values corresponded to minimal defect formation. This trend highlights the sensitivity of the energy metric to ordered texture patterns and underscores its relevance for assessing forming quality as a function of fabric angle.

Finally, although forming-induced wrinkling is governed by nonlinear mechanical phenomena such as buckling and shear–tension coupling [50], the primary objective of this study was to assess whether macroscopic wrinkle severity metrics could be statistically predicted from experimentally measured fabric parameters. The observed predictive performance (test R^2 up to 0.81 for dissimilarity and homogeneity) indicates that, within the investigated parameter space, first-order linear relationships provide an accurate approximation given the limited dataset. Exploration of more advanced nonlinear models will be conducted in future work as the dataset expands.

Conclusion

This study demonstrated a machine learning–based framework to predict forming-induced defects in flax woven fabrics using 3D scanning and Haralick texture analysis. By combining fabric geometrical parameters, mechanical properties, and wrinkle distribution quantification, the approach provided a reliable assessment of formability (namely, the surface quality upon forming). Experimental results showed that flax twill fabrics exhibited the lowest formability, while glass fiber and biaxial NCF fabrics formed more smoothly, with orientation and layer count significantly influencing wrinkle severity.

Linear regression models achieved high predictive accuracy, with an average test set R^2 of 0.81 across 10 Monte Carlo cross-validation iterations, demonstrating that integrating image-based texture analysis with fabric geometrical and mechanical parameters enables quantitative and consistent prediction of forming performance. Among the Haralick features, lower homogeneity values corresponded to pronounced wrinkles along the square-tool sides, highlighting its ability to indicate surface quality and forming consistency. Dissimilarity feature captured both defect severity and fabric architecture effects, with glass reinforcements showing lower values and the FBX350 reinforcement higher values.

It should be noted that the in-plane tension stiffness measured in this study reflects small-strain behavior, representing a limitation of this work. During forming, fabrics may experience larger strains, particularly near high-curvature or sharp-edged tools, where nonlinear effects such as fiber reorientation, strain-rate dependency, and microstructural characteristics can significantly influence the reinforcement response. These effects were not explicitly accounted for and should be incorporated in future investigations.

Future work will extend the proposed modeling framework by incorporating additional natural fiber types and advanced machine learning strategies to improve predictive accuracy. Generalization

to complex tool geometries is currently under investigation through integration of 3D-scanned point cloud reference meshes, replacing tool-specific analytical formulations. Scaling up to industrial forming scenarios and implementing real-time defect monitoring strategies can further enhance the applicability and robustness of this approach for sustainable composite manufacturing.

References

[1] W. Lee, M.K. Um, J.H. Byun, P. Boisse, J. Cao, Numerical study on thermo-stamping of woven fabric composites based on double-dome stretch forming, International Journal of Material Forming 3 (2010) 1217–1227. https://doi.org/10.1007/s12289-009-0668-5.

[2] Armin Rashidi Mehrabadi, Towards mitigation of wrinkles during forming of woven fabric composites: an experimental characterization, University of British Columbia, 2016.

[3] T. Gereke, O. Döbrich, M. Hübner, C. Cherif, Experimental and computational composite textile reinforcement forming : A review, Composites Part A 46 (2013) 1–10. https://doi.org/10.1016/j.compositesa.2012.10.004.

[4] R. Bai, B. Chen, J. Colmars, P. Boisse, Physics-based evaluation of the drapability of textile composite reinforcements, Compos. B Eng. 242 (2022) 1–15. https://doi.org/10.1016/j.compositesb.2022.110089.

[5] P. Harrison, L.F. Gonzalez Camacho, Deep draw induced wrinkling of engineering fabrics, Int. J. Solids Struct. 212 (2021) 220–236. https://doi.org/10.1016/j.ijsolstr.2020.12.003.

[6] P. Boisse, N. Hamila, E. Vidal-Sallé, F. Dumont, Simulation of wrinkling during textile composite reinforcement forming. Influence of tensile, in-plane shear and bending stiffnesses, Compos. Sci. Technol. 71 (2011) 683–692. https://doi.org/10.1016/j.compscitech.2011.01.011.

[7] A. Nazemi, Dynamic, particle-based simulation of industrial handling and draping process of textile semi-finished products, 2022.

[8] S.K. Mazumdar, Composites manufacturing: materials, product, and process engineering, 1st ed., CRC Press, 2001. https://doi.org/https://doi.org/10.1201/9781420041989.

[9] S. Kawabata, M. Niwa, H. Kawai, 4 - The finite-deformation theory of plain-weave fabrics. Part II: the uniaxial-deformation theory, Journal of the Textile Institute 64 (1973) 47–61. https://doi.org/http://dx.doi.org/10.1080/00405007308630417.

[10] Y.M. Fei, The Prediction of Wrinkle Formation in Non-crimp Fabrics during Double Diaphragm Forming, Master, University of Nottingham, 2021.

[11] J.S. Lee, S.J. Hong, W.R. Yu, T.J. Kang, The effect of blank holder force on the stamp forming behavior of non-crimp fabric with a chain stitch, Compos. Sci. Technol. 67 (2007) 357–366. https://doi.org/10.1016/j.compscitech.2006.09.009.

[12] S. Chen, O.P.L. McGregor, L.T. Harper, A. Endruweit, N.A. Warrior, Defect formation during preforming of a bi-axial non-crimp fabric with a pillar stitch pattern, Compos. Part A Appl. Sci. Manuf. 91 (2016) 156–167. https://doi.org/10.1016/j.compositesa.2016.09.016.

[13] A. Schnabel, T. Gries, Production of non-crimp fabrics for composites, n.d.

[14] S.E. Arnold, M.P.F. Sutcliffe, W.L.A. Oram, Experimental measurement of wrinkle formation during draping of non-crimp fabric, Compos. Part A Appl. Sci. Manuf. 82 (2016) 159–169. https://doi.org/10.1016/j.compositesa.2015.12.011.

[15] P. Ouagne, D. Soulat, J. Moothoo, E. Capelle, S. Gueret, Complex shape forming of a flax woven fabric ; analysis of the tow buckling and misalignment defect, Composites Part A 51 (2013) 1–10. https://doi.org/10.1016/j.compositesa.2013.03.017.

[16] P. Ouagne, D. Soulat, P. Evon, S. Renouard, M. Ferreira, L. Labonne, A.R. Labanieh, E. Laine, E. De Luycker, Use of bast fibres including flax fibres for high challenge technical textile applications. Extraction, preparation and requirements for the manufacturing of composite reinforcement fabrics and for geotextiles, in: Handbook of Natural Fibres, Elsevier Ltd, 2020: pp. 169–204. https://doi.org/10.1016/B978-0-12-818782-1.00005-5.

[17] F. Omrani, P. Wang, D. Soulat, M. Ferreira, P. Ouagne, Analysis of the deformability of flax-fibre nonwoven fabrics during manufacturing, Compos. B Eng. 116 (2017) 471–485. https://doi.org/10.1016/j.compositesb.2016.11.003.

[18] P. Wang, X. Legrand, P. Boisse, N. Hamila, D. Soulat, Experimental and numerical analyses of manufacturing process of a composite square box part: Comparison between textile reinforcement forming and surface 3D weaving, Compos. B Eng. 78 (2015) 26–34. https://doi.org/10.1016/j.compositesb.2015.03.072.

[19] H. Shen, L. Yao, X. Legrand, P. Wang, Characterization of wrinkle morphologies by surface waviness evaluation method during deep forming of multilayer composite preforms, Compos. Struct. 306 (2023) 1–13. https://doi.org/10.1016/j.compstruct.2022.116586.

[20] K. Potter, B. Khan, M. Wisnom, T. Bell, J. Stevens, Variability , fibre waviness and misalignment in the determination of the properties of composite materials and structures, Compos. Part A Appl. Sci. Manuf. 39 (2008) 1343–1354. https://doi.org/10.1016/j.compositesa.2008.04.016.

[21] O.P.L. Mcgregor, S. Chen, L.T. Harper, A. Endruweit, N.A. Warrior, Defect reduction in the double diaphragm forming process, in: 21st International Conference on Composite Materials, 2017: pp. 1–11.

[22] C. Zimmerling, C. Poppe, O. Stein, L. Kärger, Optimisation of manufacturing process parameters for variable component geometries using reinforcement learning, Mater. Des. 214 (2022) 110423. https://doi.org/10.1016/j.matdes.2022.110423.

[23] V. Daghigh, H. Daghigh, T.E. Lacy, M. Naraghi, Review of machine learning applications for defect detection in composite materials, Machine Learning with Applications 18 (2024) 100600. https://doi.org/10.1016/j.mlwa.2024.100600.

[24] L. Bin Tan, N.D.P. Nhat, Prediction and Optimization of Process Parameters for Composite Thermoforming Using a Machine Learning Approach, Polymers (Basel). 14 (2022). https://doi.org/10.3390/polym14142838.

[25] S. Kazemi, A.S. Milani, A preliminary step toward intelligent forming of fabric composites: Artificial intelligence-based fiber distortions monitoring, Eng. Appl. Artif. Intell. 133 (2024). https://doi.org/10.1016/j.engappai.2024.108262.

[26] S. Yoon, A. (Song-Kyoo) Kim, W.J. Cantwell, C.Y. Yeun, C.S. Cho, Y.J. Byon, T.Y. Kim, Defect detection in composites by deep learning using solitary waves, Int. J. Mech. Sci. 239 (2023). https://doi.org/10.1016/j.ijmecsci.2022.107882.

[27] A. Djavadifar, J.B. Graham-Knight, M. Körber, P. Lasserre, H. Najjaran, Automated visual detection of geometrical defects in composite manufacturing processes using deep convolutional neural networks, J. Intell. Manuf. 33 (2022) 2257–2275. https://doi.org/10.1007/s10845-021-01776-1.

[28] L. Lu, J. Hou, S. Yuan, X. Yao, Y. Li, J. Zhu, Deep learning-assisted real-time defect detection and closed-loop adjustment for additive manufacturing of continuous fiber-reinforced polymer composites, Robot. Comput. Integr. Manuf. 79 (2022). https://doi.org/10.1016/j.rcim.2022.102431.

[29] F.T. Peirce, 26 - The “handle” of a cloth as a measurable quantity, Journal of the Textile Institute Transactions 21 (1930) T377–T416. https://doi.org/http://dx.doi.org/10.1080/19447023008661529.

[30] ASTM International, ASTM D1388-23: Standard Test Method for Stiffness of Fabrics, (2023). https://doi.org/10.1520/D1388-23.3.2.

[31] R. Sourki, B. Crawford, R. Vaziri, A.S. Milani, Meso-level bending/reverse-bending analysis of dry woven fabrics: Observing an irreversible behavior during forming, Compos. Struct. 282 (2022). https://doi.org/10.1016/j.compstruct.2021.115124.

[32] O. Rozant, P.E. Bourban, J.A.E. Manson, Drapability of dry textile fabrics for stampable thermoplastic preforms, Compos. Part A Appl. Sci. Manuf. 31 (2000) 1167–1177. https://doi.org/https://doi.org/10.1016/S1359-835X(00)00100-7.

[33] J.Z. Yu, Z. Cai, F.K. Ko, Formability of textile preforms for composite applications. Part 1: Characterization experiments, Composites Manufacturing 5 (1994) 113–122. https://doi.org/https://doi.org/10.1016/0956-7143(94)90062-0.

[34] ASTM International, ASTM D5035-11: Standard Test Method for Breaking Force and Elongation of Textile Fabrics (Strip Method), (2019). https://doi.org/10.1520/D5035-11R19.2.

[35] A. Gasser, P. Boisse, S. Hanklar, Mechanical behaviour of dry fabric reinforcements. 3D simulations versus biaxial tests, n.d. www.elsevier.com/locate/commatsci.

[36] X.Q. Peng, J. Cao, A continuum mechanics-based non-orthogonal constitutive model for woven composite fabrics, Compos. Part A Appl. Sci. Manuf. 36 (2005) 859–874. https://doi.org/10.1016/j.compositesa.2004.08.008.

[37] Y. Shi, S. Hofmann, R. Jemmali, S. Hackemann, D. Koch, Determination of elastic properties for a wound oxide ceramic composite, Journal of Ceramic Science and Technology 5 (2014) 31–38. https://doi.org/10.4416/JCST2013-00028.

[38] J. Cao, R. Akkerman, P. Boisse, J. Chen, H.S. Cheng, E.F. De Graaf, J.L. Gorczyca, P. Harrison, G. Hivet, J. Launay, W. Lee, L. Liu, S. V Lomov, A. Long, E. De Luycker, F. Morestin, J. Padvoiskis, X.Q. Peng, J. Sherwood, T. Stoilova, X.M. Tao, I. Verpoest, A. Willems, J. Wiggers, T.X. Yu, B. Zhu, Characterization of mechanical behavior of woven fabrics : Experimental methods and benchmark results, Composites : Part A 39 (2008) 1037–1053. https://doi.org/10.1016/j.compositesa.2008.02.016.

[39] Drew Baden, Superellipse, 2024. https://physics.umd.edu/hep/drew/Math/superellipse.html#:~:text=Super%20Ellipse,outward%20curving%2C%20like%20a%20rhombus. (accessed January 16, 2026).

[40] N. Zayed, H.A. Elnemr, Statistical Analysis of Haralick Texture Features to Discriminate Lung Abnormalities, Int. J. Biomed. Imaging 2015 (2015). https://doi.org/10.1155/2015/267807.

[41] Y. Park, J.M. Guldmann, Measuring continuous landscape patterns with Gray-Level Co-Occurrence Matrix (GLCM) indices: An alternative to patch metrics?, Ecol. Indic. 109 (2020). https://doi.org/10.1016/j.ecolind.2019.105802.

[42] G. Shan, Monte Carlo cross-validation for a study with binary outcome and limited sample size, BMC Med. Inform. Decis. Mak. 22 (2022). https://doi.org/10.1186/s12911-022-02016-z.

[43] M. Komeili, A.S. Milani, On effect of shear-tension coupling in forming simulation of woven fabric reinforcements, Compos. B Eng. 99 (2016) 17–29. https://doi.org/10.1016/j.compositesb.2016.05.004.

[44] I. Taha, Y. Abdin, S. Ebeid, Comparison of picture frame and Bias-Extension tests for the characterization of shear behaviour in natural fibre woven fabrics, Fibers and Polymers 14 (2013) 338–344. https://doi.org/10.1007/s12221-013-0338-6.

[45] J.S. Lightfoot, M.R. Wisnom, K. Potter, A new mechanism for the formation of ply wrinkles due to shear between plies, Compos. Part A Appl. Sci. Manuf. 49 (2013) 139–147. https://doi.org/10.1016/j.compositesa.2013.03.002.

[46] P. Boisse, J. Colmars, N. Hamila, N. Naouar, Q. Steer, Bending and wrinkling of composite fiber preforms and prepregs. A review and new developments in the draping simulations, Compos. B Eng. 141 (2018) 234–249. https://doi.org/10.1016/j.compositesb.2017.12.061.

[47] I. Vrbik, S.J. Van Nest, P. Meksiarun, J. Loeppky, A. Brolo, J.J. Lum, A. Jirasek, Haralick texture feature analysis for quantifying radiation response heterogeneity in murine models observed using Raman spectroscopic mapping, PLoS One 14 (2019). https://doi.org/10.1371/journal.pone.0212225.

[48] D.L. Campbell, H. Kang, S. Shokouhi, Application of Hharalick texture features in brain [18F]-florbetapir positron emission tomography without reference region normalization, Clin. Interv. Aging 12 (2017) 2077–2086. https://doi.org/10.2147/CIA.S143307.

[49] C.E. Honeycutt, R. Plotnick, Image analysis techniques and gray-level co-occurrence matrices (GLCM) for calculating bioturbation indices and characterizing biogenic sedimentary structures, Comput. Geosci. 34 (2008) 1461–1472. https://doi.org/10.1016/j.cageo.2008.01.006.

[50] P. Harrison, F. Abdiwi, Z. Guo, P. Potluri, W.R. Yu, Characterising the shear-tension coupling and wrinkling behaviour of woven engineering fabrics, Compos. Part A Appl. Sci. Manuf. 43 (2012) 903–914. https://doi.org/10.1016/j.compositesa.2012.01.024.

The publication of this article was funded by the University of British Columbia 10.13039/501100005247